In Tandem Contact-Transfer Printing for High-Performance Transient Electronics

Abhishek Singh Dahiya, Adamos Christou, João Neto, Ayoub Zumeit, Dhayalan Shakthivel, and Ravinder Dahiya*

High-performance flexible electronics developed with resource efficient printing route will transform the way future electronics is manufactured and used to advance applications such as healthcare, Internet of Things, wearables, consumer electronics, etc. Herein, an innovative approach is presented that involves, for the first time, the in-tandem use of contact and transfer printing methods to realize high-quality electronic layers at selected locations on rigid (Si/SiO$_2$), flexible (polyimide), and biodegradable (magnesium (Mg) foils). Superior grade quality of printed electronic layers is demonstrated by realizing transistors and printed UV photodetectors (PDs) employing high-resolution electrohydrodynamic printing. The all-printed PDs show extremely high performance for UV detection, with extraordinary high responsivity (>10^7 A W^{-1}) and specific detectivity ($\approx$10^{17} Jones) values at low UV intensity of 0.1 µW cm^{-2}. Finally, the fabricated PDs on Mg foil are dissolved in deionized water at room temperature. Thus, in-tandem contact and transfer printing has potential for ecofriendly development of transient electronics. Further, the approach allows printing of wide range of nanomaterials and heterostructures or complex superlattice structures, which can open exciting new possibilities for high-performance electronics.

1. Introduction

The impressive progresses made in the field of flexible/bendable electronics has paved the path for the development of next-generation technologies such as rollable displays,[1] flexible sensors,[2] soft robotics,[2a,2b] wearable systems,[3] electronic-skin,[4] epidermal electronics,[5] mobile healthcare,[6] natively flexible processing engines,[7] etc. This will also have an impact on how various current information and communication technologies (ICT) will be developed in the future. There is already a

visible shift from integrated circuits (ICs) on conventional rigid silicon towards their ultrathin counterparts[8] and hybrid or heterogeneous integration, combining silicon technology with printed electronics.[9] In particular, printed electronics has opened interesting opportunities for flexible electronics as it offers excellent features such as design flexibility (maskless designs), efficient use of materials, low fabrication cost, low-temperature deposition, and possibility to realize devices on diverse nonconventional and degradable substrates.[10] The burgeoning printed electronics field however has few existing challenges such as modest performance with respect to conventional electronics, as a result of which its commercial applications are restricted to low-end.[10e] Innovative methods are much needed to push the performance of printed electronics and use this resource efficient route to develop faster device and circuits for high-end applications.

To this end, transfer printing of 1D inorganic nanostructures has shown some potential.[11] It allows transfer of laterally aligned photolithography-defined arrays of inorganic semiconducting nanostructures from donor substrate to the target flexible substrate using elastomeric stamps (**Figure 1**a). To enhance the printing efficiency and registration, modified transfer printing methods involving the interface engineering,[12] thermal modulation and kinetically controlled velocity,[13] laser driven,[14] intermetallic wetting effect,[15] and direct roll transfer[11a,11b] have been proposed. These modified transfer methods have extended the printing capacities to: i) selective transfer,[16] ii) arbitrary substrate integration,[17] iii) 3D patterning of stretchable liquid metals,[15] and iv) deterministic assembly of nano to chip scale structures.[10e,12b,18] These printing approaches have led to the development of various high-performance devices on flexible and stretchable substrates, including both n- and p-channel transistors[11a,11b] needed to present a viable alternative for conventional complementary metal-oxide-semiconductor (CMOS) electronics, and functional liquid metal circuit are designed for fabricating 3D electronic devices and sensors.[15] However, transfer printing method suffers from limitations such as choice of active material limited by the availability of a bulk-wafer from where lithography-defined, laterally aligned nanostructures are

A. S. Dahiya, A. Christou, J. Neto, A. Zumeit, D. Shakthivel, R. Dahiya
Bendable Electronics and Sensing Technologies (BEST) Group
University of Glasgow
Glasgow G12 8QQ, UK
E-mail: ravinder.dahiya@glasgow.ac.uk

The ORCID identification number(s) for the author(s) of this article can be found under https://doi.org/10.1002/aelm.202200170.
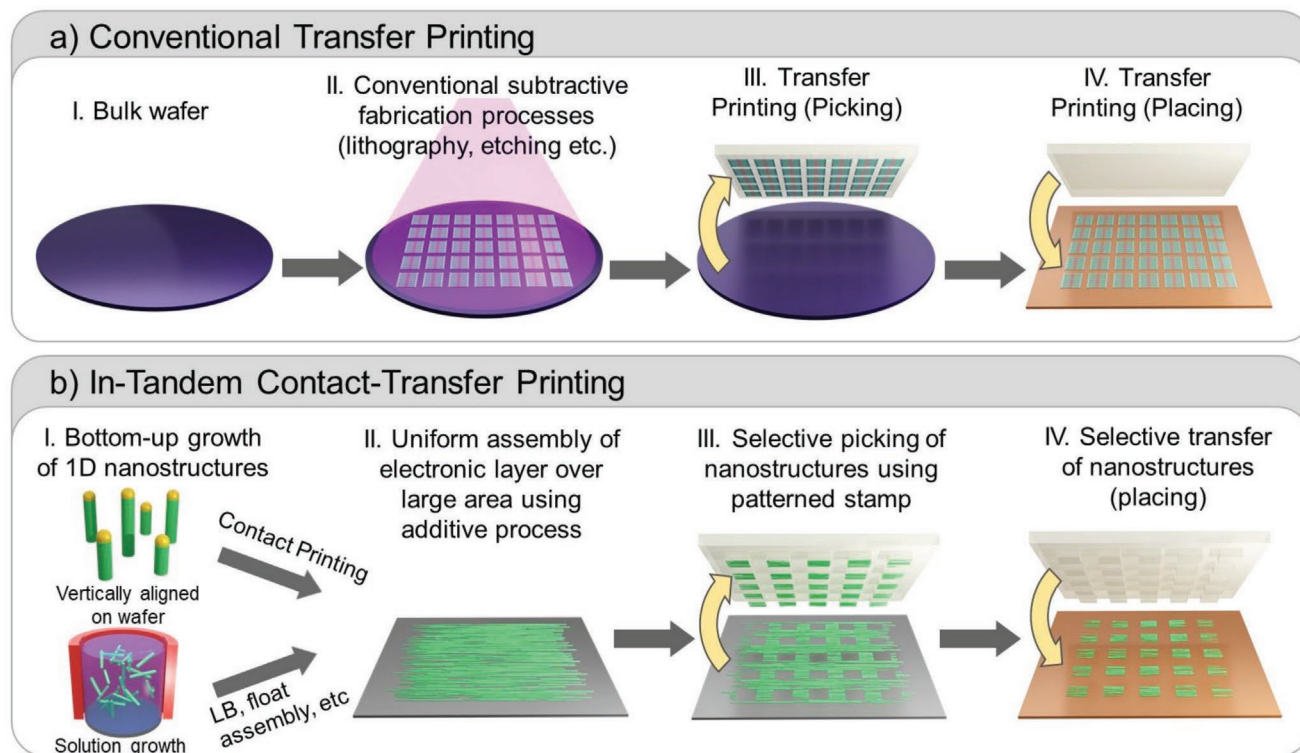
Figure 1. Schematic illustration of the steps involved in the developed in-tandem contact-transfer printing and its comparison with the conventional transfer printing: a) conventional transfer printing steps which include i) selection of an appropriate bulk wafer, ii) conventional microfabrication processes such as photolithography, etching etc. to define the morphology and dimensions of nanostructures, iii) picking-up of defined nanostructures using elastomeric stamps and iv) releasing/placing of nanostructures over target substrates. b) In-tandem contact-transfer printing steps include i) bottom-up growth of nanostructures using physical and chemical methods, ii) uniform assembly of nanostructures over an intermediate substrate employing nanoscale assembly technique such as contact printing, Langmuir–Blodgett (LB) method etc., iii) selective picking-up of nanostructures using patterned viscoelastic stamps with pillars, and iv) transfer printing (placing) of nanostructures from stamp to target device substrate at selective locations.

harvested. Such materials related limitations could be overcome by alternative nanostructure assembly methods such as Langmuir–Blodgett (LB) method,[19] and contact printing,[20] etc., which exploit bottom-up grown nanomaterials to realize nanoscale electronic layers on various substrates. The bottom-up route for nanomaterials is attractive as it allows compositional control and thus heterostructures or complex superlattice structures can also be printed. For example, dopant materials, such as phosphine for silicon, can be introduced and removed repeatedly throughout the nanowire growth, producing superlattice structures with modulated electronic properties,[21] which can be utilized to encode unconventional electronic properties and a wide variety of shapes and structures that can be used for development of various sensing, photonics, electronics and memory devices on large area flexible substrates. This means that electronic layers with richer materials systems could be obtained with contact printing or other nanoscale assembly technique and subsequently transfer printing could be used for further processing to develop devices with unique features. In doing so, the dependence on inherently wasteful conventional fabrication processes[22] (e.g., photolithography and etching to obtain nanostructures from wafers) can also be reduced.

Herein, we use this new contact-transfer printing in tandem approach, as shown in the Figure 1b, to develop

high-performance electronic devices. First, the contact printing is used to print highly laterally aligned 1D structures on an intermediate substrate to obtain uniform electronic layers. Then, conventional, or modified transfer printing is employed to selectively remove the electronic layers and print them on the final substrate. The electronic layers on final substrates are further processed to develop devices such as transistors and photodetectors (PDs). With this novel approach, we present a resource-efficient process for high-performance nanowire (NW)-based printed, transient electronics. The fabrication process steps include nanoscale material development (ZnO NWs), in-tandem use of contact and transfer printing processes, and high-resolution electrohydrodynamic (EHD) printing. All the process steps are eco-friendly, scalable, resource-efficient, and extendable for wide range of applications. First, vertically aligned ZnO NWs were grown via nontoxic Vapor Phase Transport (VPT) method using a horizontal tube furnace. Then our in-house automated contact printing system was used for uniform printing of highly dense horizontally aligned ZnO NWs on an intermediate substrate (rigid silicon).[20a,20b] Contact printing offers advantages such as: i) highly directional alignment of nanostructures, which is needed for high-device performance, ii) single-step process, iii) cost-effective, and iv) avoids contamination to NW surface as it is a dry printing method. Once NWs

2200170 (2 of 12)

based electronic layer is printed, the stamp or transfer printing was employed to transfer the electronic layers from selected locations to the final device substrate (Si/SiO$_2$, PI and Mg foil). The latter allowed us to fabricate many samples using a single donor. Printing at selective locations helps in reducing the sensor crosstalk and improves the heterogeneous integration of NW arrays.[23] It may be noted that contact printing could also be used to directly print the electronic layers at selected location, as has been demonstrated in past.[24] In fact, this would be efficient in terms of number of NW printed. However, the lithography and surface treatment needed each time to define the NW locations will make it cumbersome for large scale integration and contaminations by surface treatment step could influence the electrical properties of NWs. Further, contact printing cannot be used for nanostructures that are horizontally present on the donor substrate, for example, NWs and nanoribbons realized on silicon wafer using photolithography. In this regard, the in-tandem contact-transfer printing presented here is versatile and makes best use of both printing methods. Next, EHD printing was utilized to print diffusive Au contacts over the two ends of aligned NWs to define the device channel. EHD offers excellent possibilities such as drop-on-demand feature (resource-efficient), substrate independent patterning, compatibility with large area manufacturing, and the potential for low-cost operation.[25]

The above approach was used to develop proof-of-concept devices such as transistor and PDs. First, n-channel transistors were developed over Si/SiO$_2$ substrate to extract the electrical properties of the as-gown ZnO NWs. Next, these NWs were used to develop printed PDs. The printed PDs, on both PI and Mg, showed record high responsivity (>10^7 A W^{-1}) and specific detectivity ($\approx10^{17}$ Jones) values at low UV intensity of 0.1 µW cm^{-2}. Finally, we show that the developed PDs on Mg foil can physically disintegrate and dissolve in 240 number of days in deionized (DI) water of pH $\approx$6 at room temperature.

2. Results and Discussions

2.1. In Tandem Contact-Transfer Printing Technique

Figure 1 schematically shows the developed synergistic contact-transfer printing steps for selective transfer of NWs. To draw the comparison, Figure 1 also illustrates the processing steps for conventional transfer printing. The benefits of proposed printing approach include: i) wider choice of nanomaterial to be printed, ii) resource efficient process as it avoids repeated use of conventional microfabrication steps, iii) cost-effective, and iv) more ecofriendly. To begin with, vertically aligned ZnO NWs were grown on c-plane sapphire substrates. Bottom-up approaches by vapor-liquid-solid (VLS) mechanism using VPT technique have been successful in producing environment friendly ZnO NWs. Figure S1 (Supporting Information) shows schematic representation of the NW growth VPT system, scanning electron microscopy (SEM) images, and x-ray diffraction (XRD) scan of the as-grown ZnO NWs. Figure 1b shows high-density of highly vertically aligned ZnO NWs growth on c-plane sapphire substrates, similar to the previous reports of ZnO NW growth on (0001)-oriented hexagonal substrates.[26] It may be

noted that some of the long NWs (length > 20 µm) could bend during the growth process due to their own mechanical strain. To assess the crystallographic quality of the NWs, XRD analysis was performed. As can be seen from the XRD data (Figure S1c, Supporting Information), ZnO NWs show dominant peaks at $2\theta = 34.4°$, corresponding to (0002) plane orientation. This observation indicates growth of highly c-axis-oriented wurtzite ZnO NWs, as hinted from SEM image. High density of vertically aligned NWs is critical to achieve high density of horizontally aligned contact printed NWs and hence the uniform electronic layer.

Subsequently, contact printing was performed for uniform assembly of laterally aligned ZnO NWs over an intermediate receiver substrate. **Figure 2** schematically shows contact printing process steps, 3D system model and the SEM images of the resulting printed NW-based electronic layer. The equipment details can be obtained from our previous work.[20a] Briefly, during the printing process, the combination of a controlled vertical and shear forces (due to sliding) results in the detaching of NWs from the donor sapphire substrate and transferring onto the intermediate receiver. This results in the NWs alignment along the direction of sliding. From the no sliding test, we see that sliding is needed not only for directional alignment but for breaking as well. The details of the printing conditions are given in methods section. To achieve uniform printing of NWs, the applied pressure at the predetermined level was maintained throughout the printing process and applied evenly along the entire area of the sample. Figure 2c–e shows the SEM images of printed NW at various magnifications. By inspecting the SEM images, we observe that the uniform printing of NWs across the entire surface area ($\approx$1cm^2). This suggests that using the contact printing system with self-aligning platforms can achieve conformal contact between the donor and receiver substrates over large areas. Using SEM images and the analysis software (GTFiber2),[27] statistical analysis of the printed NWs, including the average orientation angle, mean diameter, and NW density per micrometer was obtained and is shown in Table S1 (Supporting Information). The extracted mean printed NW density is $\approx$1.3 NWs µm^{-1}. The printed high density of NWs could be correlated with the as grown NWs on donor sapphire substrate. Encouragingly, more than 93% of the printed area has shown the average NW orientation within ±5 degree of the direction of sliding (90°). This indicates a high level of NW alignment which was hinted from the SEM images. A high density of aligned NWs is indeed required for the fabrication of high-performance flexible electronics as it reduces the electron scattering at the NW-NW junction and facilitates efficient charge transport. Such a high NW alignment could also be attributed to the additional shear force applied during the printing process. To prove this hypothesis, a NW sample (silicon) was printed where no sliding motion was used (velocity = 0). The sample without sliding motion demonstrates extremely low density and large variation in alignment (Figure S2, Supporting Information).

Next, the transfer printing was employed for selective assembly of ZnO NWs on rigid Si/SiO$_2$, and flexible polyimide (PI) and biodegradable magnesium (Mg) foil from contact printed uniform electronic layers. It is to note that optimization studies for transfer printing were performed on PI substrate.
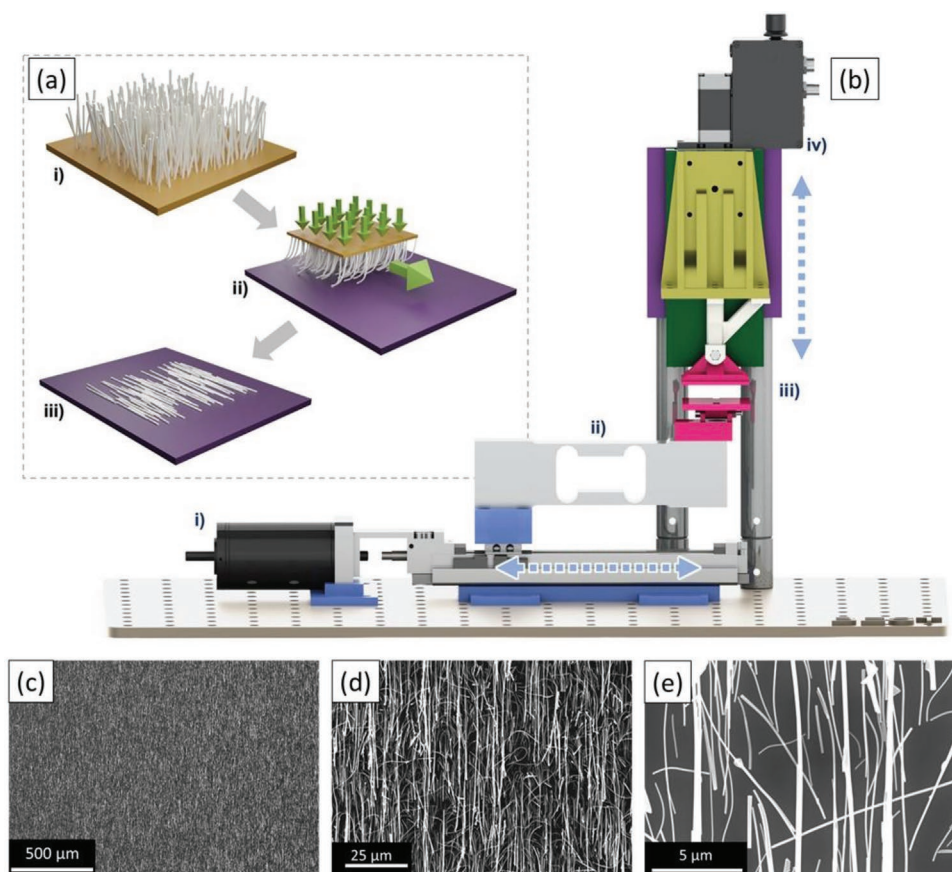
**ADVANCED
SCIENCE NEWS**

www.advancedsciencenews.com

**ADVANCED
ELECTRONIC
MATERIALS**

www.advelectronicmat.de

Figure 2. Contact printing of ZnO NWs: a) Schematic showing the process steps: i) donor with vertically grown NWs, ii) Controlled vertical pressure and sliding of donor over receiver substrate, and iii) printed and aligned NW layer. b) schematic of custom-built system: i) horizontal stage, ii) load cell, iii) self-aligning platforms, iv) vertical stage, and c–e) SEM images of the contact printed NWs at different magnifications. The contact printing concept in (a) and 3D schematic of the custom-built contact printing system in (b) are adapted from ref. [20a].

Figure 3 schematically shows the selective transfer printing steps. First, a polydimethylsiloxane (PDMS) mold with periodic square-shaped pillars was prepared from the silicon master (for details see methods). Figure S3 (Supporting Information) shows the optical microscopy images of etched silicon master template and PDMS mold with square pillar structures. From the Figure S3 (Supporting Information) we can see that the length and width of square structures are 100 and 100 µm, respectively. Using the fabricated microstructure PDMS stamp, we transferred the contact printed ZnO NWs selectively over target device substrate. To have reasonably high transfer efficiency (during the picking-up step), we used previously reported capillary-force-assisted stamp technique that uses a thin layer of evaporated water as an instant glue to increase the adhesion energy between nanomaterials and PDMS during the pick-up step.[28] To have a thin layer of water, we hold the fabricated PDMS mold over a pre-heated water at 80 °C for 10 s. Next, immediately the stamp was placed over the contact printed NWs substrate (pillar side facing NWs) and constant force of 10N was applied for 10 s. After the liquid evaporates, the NWs were transferred onto PDMS stamp. The stamp with NWs was immediately placed over the target device substrate and a constant force was applied. The yield and registration factor of printed nanomaterials are low due to the viscoelastic nature

of the PDMS stamp, but this is inherent to the conventional transfer printing. To optimize the transfer yield, the magnitude of the applied force was varied from 0.5 to 10 N. The number of NWs transferred were dependent on the magnitude of the force applied (Figure S4, Supporting Information). Increasing the applied force enhances the number of NW transferred. It is to note that due to system limitation we could not apply higher forces to further increase the transfer yield. The use of water as an adhesion promoter ensures the low contamination level on the NW materials and largely preserves their electrical properties. This is needed for the high performance offered by inorganic NWs.

2.2. N-channel Transistors and Electrical Characterizations

To confirm the material's electrical quality, ZnO NW based bottom-gated field-effect transistors (NW-FETs) were fabricated and characterized. The ZnO NW-FETs (based on printed NWs) were fabricated on Si/SiO$_2$ substrates using standard microfabrication processes. The resulting electrical characterization results, output, and transfer curves along with the ZnO NW-FET schematic are shown in **Figure 4**. It is to note that the transfer of NWs was performed using the exact procedure
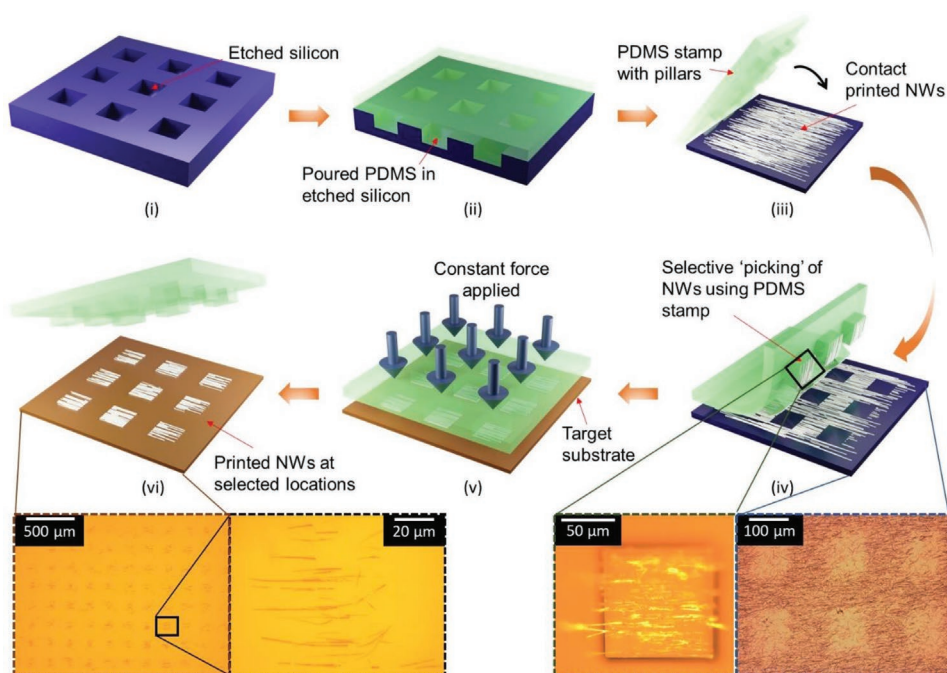
Figure 3. Schematical illustration of various steps involved in selective transfer printing of ZnO NWs from contact printed electronic layer: i) fabrication of master silicon template using photolithography and etching, ii) fabrication of PDMS stamp using master template, iii) placement of PDMS stamp with pillar structures onto contact printed NWs, iv) selective transfer of NWs onto the PDMS stamp (inset shows the optical images of PDMS stamp with transferred NWs on pillars (left) and selectively removed NWs from contact printed NWs (right)), v), PDMS stamp with NWs in conformal contact with the target device substrate and vi) selectively printed NWs over target device substrate (inset shows the optical images of the printed NWs at different magnification).

explained above. The transfer characteristics (I_{DS}–V_{GS}) with drain bias (V_{DS}) of 2 V was obtained by varying gate-source voltage (V_{GS}) from −20 to 20 V (Figure 4c). The current on/off ratio ($I_{on/off}$) was found to be >10^3 and threshold voltage (V_T) of
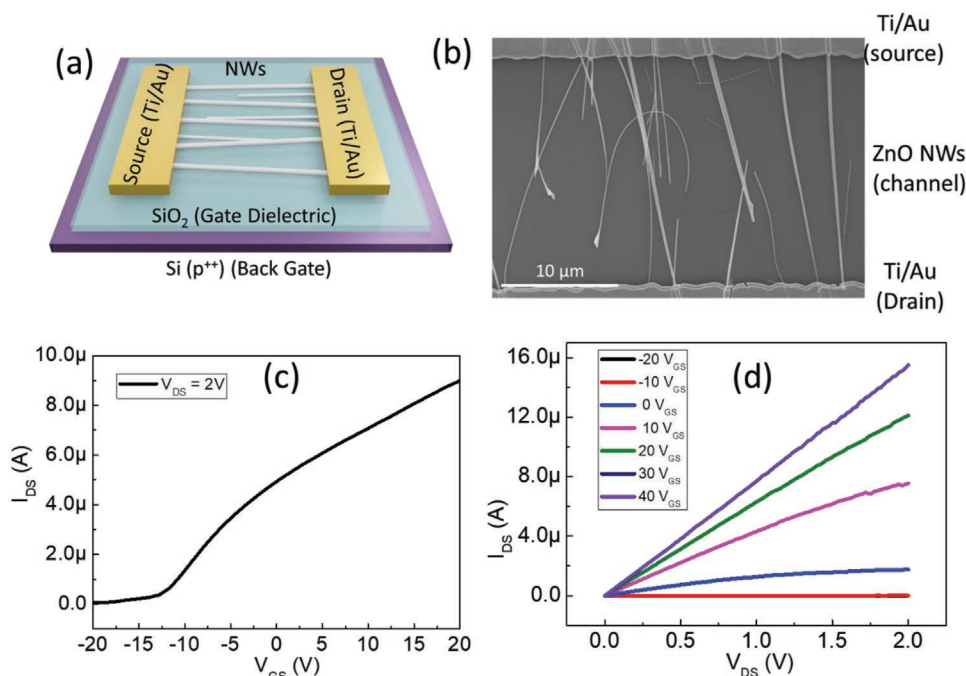

Figure 4. Electrical characterization of the ZnO NW-FETs: a) schematic of the printed array of ZnO NWs transistor, b) SEM image of a typically fabricated FET device, c) device transfer characteristics, and d) output characteristics.

© 2022 The Authors. Advanced Electronic Materials published by Wiley-VCH GmbH

**ADVANCED
SCIENCE NEWS**
www.advancedsciencenews.com

**ADVANCED
ELECTRONIC
MATERIALS**
www.advelectronicmat.de

−13 V. The extracted peak field effect mobility (μ_{FE}) was found to be ≈50 cm^2 V^{-1} s^{-1}, using the standard cylinder-plate capacitor model.[29] The extracted mobility compares well with the state of the art for ZnO NWs which confirm the high quality of our nanomaterial and in tandem printing methods. The output characteristics (V_{DS}–I_{DS}) was obtained by varying V_{GS} from −20 to 40 V with step of 10 V (Figure 4d). Notably, the low-V_{DS} region shows a linear dependence of I_{DS} with increasing V_{DS} without any inflection point (confirming formation of ohmic contacts with Ti metal). This is needed to extract the near correct values of nanomaterials. The high ohmicity of the metal-semiconductor (MS) contacts further confirms the clean transfer of NWs with negligible contamination on the NW surface.

It is to note that the fabricated transistors showed some device-to-device performance variations including V_T, mobility etc. To improve the performance reproducibility of devices from single batch or from different batches, many important aspects need attention. First, uniform ZnO NW synthesis which includes NWs having controlled diameter, doping, surface states, etc., on the donor substrate. To-date, it is highly challenging to reproduce the NW growth process with controlled electrical properties. Second, highly controlled NW printing approach to have uniform electronic layer. This will ensure similar number of NWs in the device channel. The use of an ensemble of NWs to form a device (instead of single NW) should also lead to statistically lower dimensional variations and hence improve the uniformity among devices. Lastly, NW-FETs which work in depletion/accumulation mode are heavily influenced by the quality of metal–semiconductor contact interface, dielectric/semiconductor interface quality, and adsorbed species on NWs.[30] Because of the low dimensionality of NWs, it is very challenging to realize high quality contacts primarily due to the electrostatics involved at nanocontact interfaces.[31] Currently, we are working on some of these aspects to further reduce the batch-to-batch performance variations of devices and will be presented in our future works.

2.3. Printed Photodetectors on Flexible Substrates and Electrical Characterizations

Further, we fabricated flexible PDs on PI substrate using EHD printing and performed detailed characterization (**Figure 5**). The EHD printed contact electrodes over the aligned ZnO NWs were made using the commercial Au ink (Figure 5a). Electrical measurements were performed on PDs under ambient conditions to monitor their performance. First, the current–voltage (I–V) response of a single device under dark and different UV illumination intensities is measured and results are shown in Figure 5b. For I–V measurements, the bias voltage is swept from −1 to 1 V. A typical symmetrical nonlinear behavior was observed for the fabricated PD device. This is because Au (work function −5.1 eV) is expected to form a Schottky contact on n-ZnO NWs (electron affinity ≈4.5 eV). Further, the figure shows that photocurrent increases from ≈0.5 μA (dark current) to ≈5 μA (2 μW cm^{-2}) in 365 nm UV light (one order change in photocurrent) at V_D = 1 V. The working mechanism for ZnO NW based PDs is well documented.[32] Briefly, in the dark condition, the absorbed oxygen molecules on the NW surface

results in the depletion of electrons. The electron depletion leads to upward band bending and an electric barrier across the MS interface. When illuminated with UV light, the separation of photogenerated electron-hole pairs leads to the desorption of oxygen molecules and thus, increase in the concentration of free electrons. This will also result in the decrease of MS barrier. Both phenomenon results in an enhancement of drain current.

The I–V measurements shown in Figure 5b confirm that the device can be operated at low drain voltages. Accordingly, low bias voltage (V_D = 1) is applied to measure time-resolved photoresponse with varying UV intensity from 0.1 to 2.0 μW cm^{-2} (Figure 5c). The PD shows a reasonably high response to the UV light intensity, like Figure 5b. Furthermore, repeated dark-UV response cycles were performed at intensity of 0.5 μW cm^{-2}. The obtained set of data showed good repeatability (Figure 5d). Using this data, rise and recovery time is calculated. A response (15 s) and recovery (30 s) time are exhibited by the printed UV sensor. Further, other important parameters including responsivity (R), specific detectivity (D^*), external quantum efficiency (EQE), and I_{Light}/I_{Dark} ratio are extracted from the time-resolved photoresponse curves at different UV intensity to further evaluate the performances of printed PDs. First, the R of printed PDs was calculated using equation (1)[33]

$$R = \frac{\left(I_{Light} - I_{Dark}\right)}{\left(P_{in} \times S\right)} \tag{1}$$

where I_{Light} represents the current under UV light illumination; I_{Dark} is the current under dark condition; P_{in} is the incident light power per unit area and S is the effective sensing area of the device. It can be seen from this set of data (Figure 5e); responsivity monotonically decreases with increasing UV intensity. At low UV intensity (0.1 μW cm^{-2}), a maximum responsivity of 8×10^7 was achieved (for $S = 1.8 \times 10^{-7}$ cm^2, considering NWs as cylindrical structure with diameter 100 nm). At higher UV intensities, the R values decreases but remained more than 10^7. In addition, the D^* is another important PD parameter which is given by[33]

$$D^* = \frac{R}{\sqrt{2eJ_D}} \tag{2}$$

where e is the elementary charge and J_D is dark current density. The detectivity indicates the capability of PDs to detect small signals. Like responsivity, the D^* dependent of applied UV intensity curve (Figure 5f) exhibits the same trend. The D^* reaches maximum value of 8×10^{16} Jones at the low UV illumination of 0.1 μW cm^{-2}. Finally, EQE, i.e., the ratio of the number of converting absorbed photons to electrons and the total number of excitation photons, was extracted from the equation below:

$$EQE = \frac{hc \times R_\lambda}{e\lambda} \times 100 \tag{3}$$

where h is Planck's constant, c is velocity of light, and λ is the wavelength of incident light. The EQE decreases gradually with increasing UV light intensity (Figure 5g). The largest EQE

ADVANCED
SCIENCE NEWS

www.advancedsciencenews.com

ADVANCED
ELECTRONIC
MATERIALS

www.advelectronicmat.de

ADVANCED
SCIENCE NEWS

www.advancedsciencenews.com

ADVANCED
ELECTRONIC
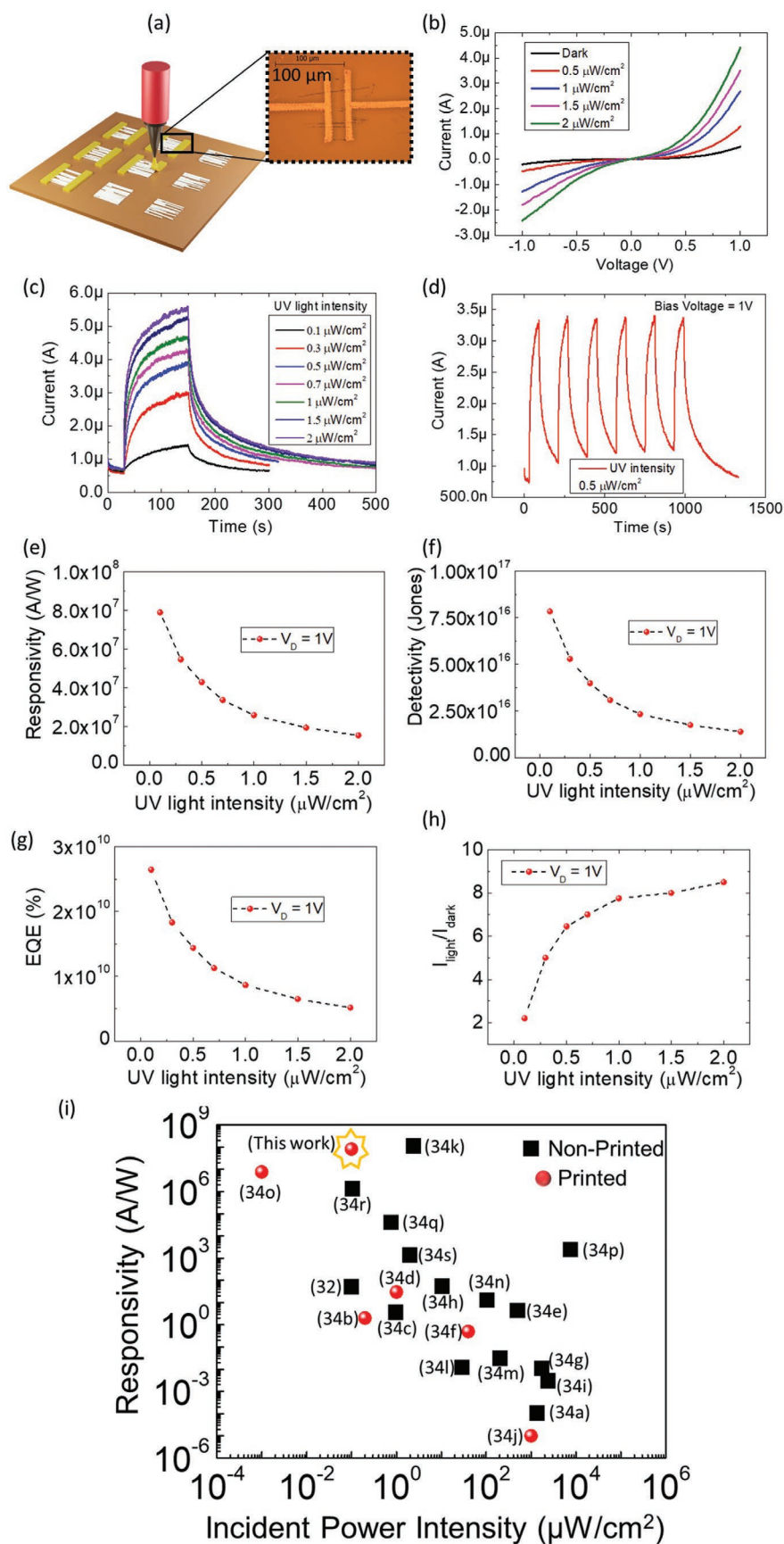**MATERIALS**

www.advelectronicmat.de

Table 1. Printed PDs performance comparison with the state-of-the-art photodetectors based on ZnO nanomaterials and other technologically important materials. N/A, data not available; NRs, nanorods; NPs, nanoparticles; SiC, silicon carbide; and GaN, gallium nitride; TPU, Thermoplastic polyurethane; QDs, Quantum dots.

Materials	EQE [%]	Specific detectivity [Jones]	Responsivity [A W^{-1}]	I_{Light} /I_{Dark} ratio (Peak)	Resource-efficient fabrication	Response/Recovery times [s]	Ref.
ZnO NWs	N/A	8.14×10^8	$\approx 10^{-5}$	13.4	Yes (Printing)	N/A	[34j]
ZnO NWs	N/A	N/A	54	>10^5	No	0.2 / 0.1	[32]
ZnO NWs	N/A	3.3×10^{17}	7.5×10^6	>10^5	Yes (Printing)	0.56 / 0.32	[34o]
ZnO NRs	N/A	N/A	$\approx 10^{-4}$	>10^3	No	49 / 25	[34a]
ZnO porous film	N/A	N/A	0.5	10^6	Yes (Printing)	0.4/1.3	[34f]
ZnO NWs	N/A	N/A	4.5×10^4	>10^4	No	N/A/1	[34q]
ZnO NWs	N/A	N/A	2.6×10^3	>10^5	No	N/A/0.28	[34p]
ZnO NWs	N/A	>10^{18}	1.2×10^6	>10^7	No	1/N/A	[34r]
ZnO NWs/TPU composite	N/A	N/A	30	>10^2	Yes (Printing)	0.8/1.6	[34d]
ZnO NWs	1.3×10^3	3.2×10^{14}	4	$\approx 10^4$	No	1.8/1.7	[34e]
ZnO–Ga$_2$O$_3$ Hetero structures	N/A	6.3×10^{12}	1670	N/A	No	$10^{-4}/10^{-3}$	[34g]
ZnO QDs—Graphene Hetero structures	N/A	10^{14}	>10^8	1.7	No	5/85	[34k]
Graphene Nanoplatelet/ ZnO Hetero structures	N/A	2×10^{11}	2.2	10^2–10^3	Yes (Printing)	9.6/17.2	[34b]
ZnO NPs	N/A	N/A	12	>10^5	No	250/150	[34n]
Gallium Oxide	N/A	10^{12}	≈ 30	>10^4	No	N/A	[36]
GaN	N/A	5.3×10^{14}	10^4	N/A	No	>20 / 60	[37]
SiC	N/A	N/A	0.18	N/A	No	14 / 60	[38]
ZnO NWs	2.5×10^{10}	8×10^{16}	8×10^7	≈ 9	Yes (Printing)	15 / 30	(This work)

reaches 2.5×10^{10}% under 0.1 μW cm^{-2} of UV intensity. These results indicate that the obtained printed PDs have outstanding UV detectivity. Finally, I_{Light}/I_{Dark} ratio was extracted and shown in Figure 5h. The extracted I_{Light}/I_{Dark} ratio showed opposite increasing trend compared to R, D* and EQE with an increase of UV intensity. At higher UV intensity (2 μW cm^{-2}), the ratio increases to ≈9 from ≈2 under 0.1 μW cm^{-2}.

The PD device performance is compared with the state-of-the-art ZnO nanomaterials-based UV detectors (**Table 1** and Figure 5i).[32,34] The systematic studies shown above have confirmed the high performance of the all-printed PDs based on ZnO NWs which is comparable to the reported record for ZnO NWs. Particularly, they have shown the detectivity values comparable to the best reported printed PDs based on ZnO NWs.[34o] Furthermore, the obtained R value is among the best performance in reported ZnO-based printed and nonprinted PDs (Figure 5i). However, the I_{Light}/I_{Dark} ratio is significantly lower than the state-of-the-art reports. This could be enhanced by increasing the NWs in the channel and decreasing the

doping concentration in ZnO NWs to have higher Schottky barrier energy.[34o] Higher potential barrier at MS contact will help to decrease the level of dark current which also helps in terms of enhancing the detectivity value of the PD. Despite low I_{Light}/I_{Dark} ratio, such a high PD performance could be attributed to the following: i) low-device area (thanks to high-resolution EHD printing), ii) efficient charge transport because of single crystallinity and excellent alignment of printed NWs, and iii) negligible impurities inclusion during contact/transfer printing (dry process), as confirmed from the transistor device electrical characterization results. Furthermore, we have compared our printed PD's performance with a similar PD device fabricated using conventional lithography (Figure S5, Supporting Information). Compared with the conventionally fabricated device (**Table 2**), printed sensor showed higher I_{Light}/I_{Dark} ratio and fast response/recovery times. But the conventionally fabricated device demonstrated approximately one order higher responsivity and EQE values than printed ones whereas comparable detectivity values are obtained for both devices. This is

Figure 5. Printed ZnO NWs-based UV photodetectors (PDs): a) schematic of EHD printing on selectively transferred ZnO NWs, b) I–V characteristics under dark and UV light at different intensities, c) response to UV light with different intensities from 0.1 to 2 μW cm^{-2}, d) cyclic response to UV intensity of 0.5 μW cm^{-2} confirming the repeatability of device performance, e) the corresponding responsivity versus incident UV light intensity, f) the corresponding detectivity versus incident UV light intensity, g) the corresponding external quantum efficiency versus incident UV light intensity, h) relationship between the I_{Light}/I_{Dark} ratio and UV light intensity, and i) Responsivity comparison of our all-printed PD with the state-of-the-art ZnO based printed and nonprinted PDs.

2200170 (8 of 12)

**ADVANCED
SCIENCE NEWS**

www.advancedsciencenews.com

**ADVANCED
ELECTRONIC
MATERIALS**

www.advelectronicmat.de

Table 2. Performance comparison for ZnO NW based PDs fabricated using different routes.

Fabrication Technology	EQE [%]	Specific detectivity [Jones]	Responsivity [A W^{-1}]	I_{Light}/I_{Dark} ratio (Peak)	Resource-efficient fabrication	Response/recovery times [s]
Conventional (Substrate- PI)	$\approx 10^{11}$	$\approx 10^{17}$	6×10^{8}	1.4	No	30/>500
EHD (Printing) (Substrate- PI)	2.5×10^{10}	8×10^{16}	8×10^{7}	≈ 9	Yes	15/30
EHD (Printing) (Substrate- Mg)	8×10^{9}	$\approx 10^{17}$	4×10^{7}	≈ 27	Yes	15/30

expected as deposited Ti/Au metal with conventional fabrication route forms nearly ideal ohmic MS contact with ZnO.[30,35] It is important to highlight here that compared with conventional fabricated devices, the present adopted printed manufacturing route is highly resource-efficient (for both active and electrode material usage).

2.4. Printed Photodetectors on Biodegradable Substrates, Electrical Characterizations, and Transience Study

Finally, we demonstrate the fabrication steps can be applied over biodegradable substrates to realize transient devices. Towards this, PDs were printed on biodegradable Magnesium (Mg) foils (≈ 20 µm thick) as device substrate and the electrical characterization results are shown in **Figure 6**. It is to note that before starting the fabrication process on Mg foil, ≈ 1 µm thick biodegradable SiO_2 was deposited to passivate the rough surface (rms ≈ 800 nm) using the plasma-enhanced chemical vapor deposition (PECVD) technique. Figure 6a shows an exploded view of various biodegradable and nonbiodegradable layers of the fabricated PDs. Magnesium is chosen as device substrate due to its inherent advantages including high thermal stability (required to anneal at 250°C to cure the printed Au electrodes), biodegradability, and biocompatibility. Following this, the previously described fabrication steps were followed to develop all printed PD. The fabricated devices were characterized under similar conditions. Time resolved photoresponse was measured at the constant UV intensity 0.1 µW cm^{-2} for different bias voltages (Figure 6b), and under different UV light intensities at fixed bias voltage of 1 V (Figure 6c). Based on the time-resolved photoresponse curves, R, D^*, EQE, and I_{Light}/I_{Dark} ratio values were extracted. It is to note that the absolute current at $V_D = 1$ V for PDs on Mg foils are different than PDs on PI (Figure 5). This is because of the difference in number on NWs in the channel. Nevertheless, the R, D^*, and EQE values are very similar. Increasing the bias voltage from 1 to 2 to 5 V there is progressive increase of the R, D^* (Figure 6d) and EQE (Figure 6e) values. The I_{Light}/I_{Dark} ratio remains almost constant (≈ 27) for all bias voltages (Figure 6f). Next, we fixed the bias voltage to 1 V and performed the time-resolved photoresponse for different UV intensities (0.1–2 µW cm^{-2}). We have further extracted and plotted the R (Figure 6g), D* (Figure 6h) and EQE (Figure 6i) values for this data. As expected, there is a decrease in the magnitude of R, D* and EQE values with the increase of UV intensity (like devices on PI). However, the decreasing trend is not similar. For the PDs on Mg, the R and EQE values remained constant up to UV intensity 0.5 µW cm^{-2} while values of D* remained constant till 0.3 µW cm^{-2}. After which the values showed consistent decreasing trend.

Previous studies to explore the dissolution behavior of biodegradable Mg metal foil has been performed in phosphate buffer solution (PBS, pH 7.4).[39] In the present study, the PDs were placed inside DI water (pH ≈ 6) at room temperature (RT) to study the transience behavior of the device and the process is schematically shown in Figure 6j,k. Figure S6 (Supporting Information) presents a series of images during the transience by hydrolysis of PDs on a Mg foil (≈ 20 µm) at various times. Day 0 (Figure S6i, Supporting Information) image represents first day when the PD was placed inside the DI water. After 10 days inside the DI water, the PD components started to disintegrate (Au electrodes observed floating in DI, see inset in Figure S6iii, Supporting Information). The disintegration starts at the interfaces between the different layers (SiO_2/Mg and SiO_2/Au). After 60 days, the PD was lifted out of the DI water and thickness monitoring was performed using an optical profilometer and SEM. The extracted thickness using the SEM images of PD device was ≈ 15 µm (Figure S7, Supporting Information). This shows the etching rate of the device (mainly Mg) is ≈ 83 nm day^{-1}. With this rate, the complete dissolution of the Mg foil would occur after ≈ 240 d under these conditions. To enhance the etching rate of the PD device, solution with higher basicity or temperature (36–37 °C) could be used.[10b] It is important to note that in the present device, the metal contacts are printed using nonbiodegradable Au electrodes. In the future work, novel biodegradable printing inks of materials such as Mg, Fe, etc. will be explored to realize all printed and fully biodegradable electronics.

3. Conclusions

We have presented a novel resource-efficient, printed electronics route to fabricate high-performance inorganic nanowire (NW)-based flexible and transient electronics. The presented approach exploits the best of both contact and transfer printing methods. Starting from the synthesis of NWs (Vapor Phase Transport process) to their integration process (in-tandem contact and transfer printing), and finally to define metal electrodes (electrohydrodynamic printing), greener pathways were followed. The major advantages of the proposed NW-printing approach, as compared to the conventional transfer printing, are two folds: i) no need of printing material to be available in bulk (wafer) form which will increase the range of nanomaterials that can be used for the fabrication of high-performance nanoscale devices, and ii) reduced-dependence on conventional microfabrication steps including lithography and etching which will reduce the generation of toxic chemical waste. The efficacy of the developed manufacturing route was demonstrated by fabricating transistors and high performance all-printed UV
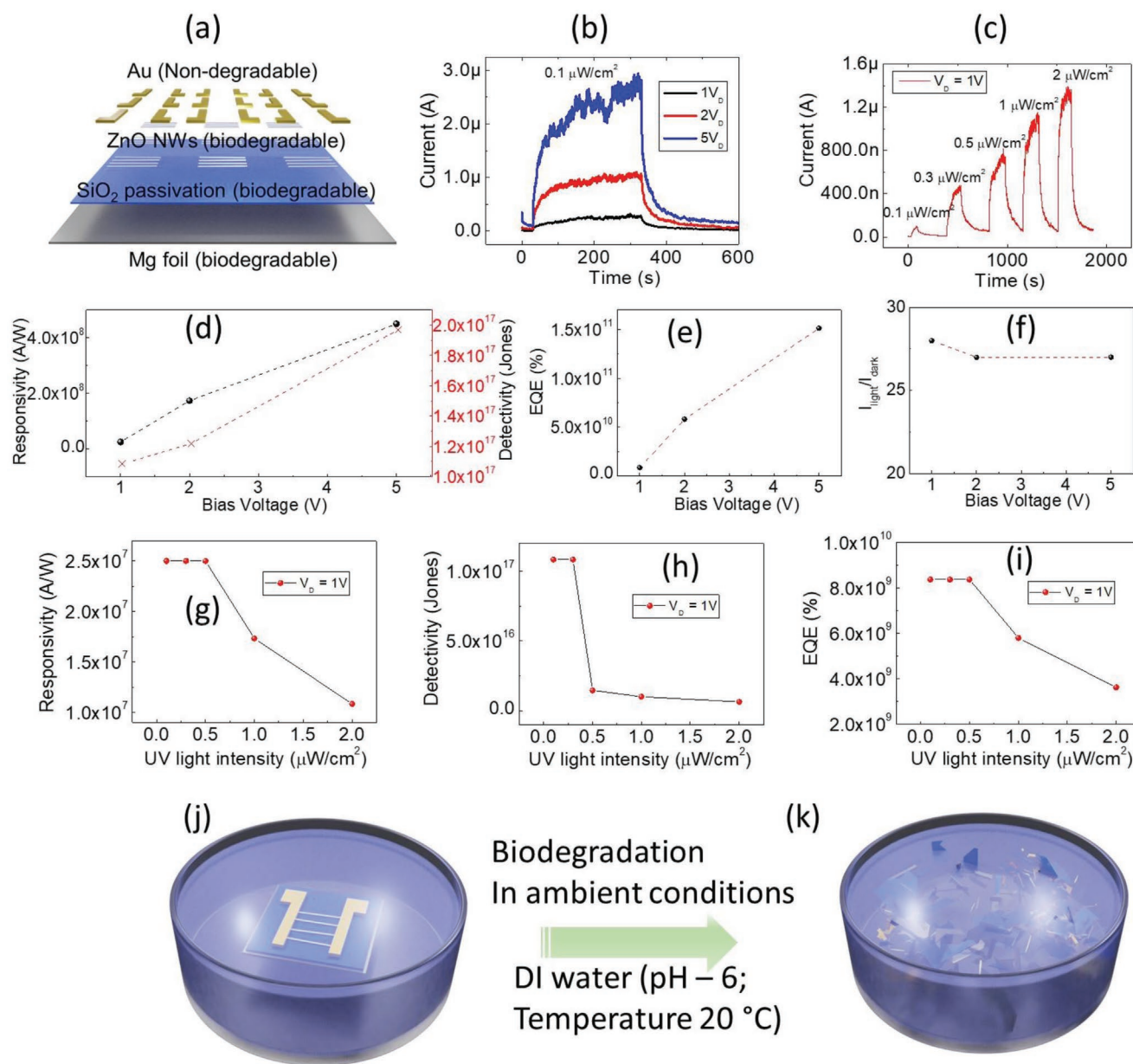
**ADVANCED
SCIENCE NEWS**

www.advancedsciencenews.com

**ADVANCED
ELECTRONIC
MATERIALS**

www.advelectronicmat.de

Figure 6. Printed ZnO NWs-based UV photodetectors on biodegradable Mg foils: a) exploded view illustration of various biodegradable and nonbiodegradable layers, b) response to UV light intensity of 0.1 µW cm^{-2} at different applied drain bias, c) response to UV light with different intensities from 0.1 µW cm^{-2} to 2 µW cm^{-2} at 1 V applied bias. Extracted PD performance metrics from data shown in (b): d) responsivity and specific detectivity, e) external quantum efficiency, and f) I_{Light}/I_{Dark} ratio. Extracted PD performance metrics from data shown in (c): g) responsivity, h) specific detectivity, and i) external quantum efficiency. j,k) schematic representation of the biodegradation behavior of the printed PDs on Mg foils in aqueous solution.

photodetectors (PDs) on flexible polyimide (PI) and biodegradable magnesium (Mg) metal foils. The PDs on both substrates (PI and Mg) showed similar high-performance for UV detection, with extremely high responsivity (>10^7 A W^{-1}), specific detectivity (≈10^{17} jones), and EQE (2.5 × 10^{10}%) values at low UV intensity of 0.1 µW cm^{-2}. The obtained PD performance was compared with the PDs fabricated using conventional microfabrication processes and shown to have better performance in terms of I_{Light}/I_{Dark} ratio and response/recovery time. The R, D*, and EQE obtained values were slightly less for all-printed PDs. Finally, the developed printed PDs on Mg

were demonstrated to disintegrate and dissolve (except printed Au) in DI water at room temperature within 240 days. The presented work opens new avenues towards NWs based high-performance, printed, and sustainable electronics.

4. Experimental Section

Vapor Phase Transport (VPT) Method: The VPT growth of ZnO NWs by vapor liquid solid (VLS) mechanism was performed inside a horizontal quartz tube furnace by carbothermal reduction of ZnO nanopowder

**ADVANCED
SCIENCE NEWS**

www.advancedsciencenews.com

**ADVANCED
ELECTRONIC
MATERIALS**

www.advelectronicmat.de

on (0001) c-plane sapphire substrates (Figure 1a).[21,34c,40] Prior to NW synthesis, the cleaned substrates were coated with Au film (3 ± 1 nm) using an electron-beam evaporator. Coated substrates and the mixture of source material (ZnO and carbon powder at 1:1 weight ratio) are placed in an alumina "boat," which is inserted inside a high temperature furnace. The samples were heated in an Ar ambient at 950 °C (growth on sapphire) for 120 min for the growth of ZnO NWs in the sub-100 diameter range.

Morphological and Structural Characterizations: The morphological analysis of as grown and contact printed ZnO NWs is performed using scanning electron microscopy (SEM- Hitachi SU8240). ZnO NWs crystallinity was studied using X-ray diffraction (XRD) with Cu Kα_1 radiation on the Bruker D8 Venture kappa geometry diffractometer equipped with a Photon-II CPAD detector. The scans were performed in the 2θ range from 30° to 40° at a scanning rate of 0.01° s^{-1}.

Contact Printing: To carry out the NW printing, a well-controlled custom-built contact printing system was used (Figure 2a,b). The details of the developed system are reported elsewhere.[20a] In the contact printing process, a flat rigid donor substrate with vertically grown ZnO NWs was brought into physical contact with a receiver substrate. Then, a controlled uniform pressure is exerted between the donor and receiver and subsequently the donor substrate is slide over the receiver while maintaining the applied pressure. In the present study, the donor sample (NWs on sapphire) was used to print NWs on a Si receiver substrate. The printing pressure and sliding velocity were set to be 33 kPa and 1 mm s^{-1}, respectively.

Transfer Printing: The selective printing of the array of aligned ZnO NWs was carried out using controlled transfer printing (Figure 3). To prepare a master template, periodic square hollow structures were fabricated on a silicon wafer. To realize the structures, a positive-type photoresist was patterned using photolithography. Following, the silicon was etched by employing deep reactive ion etching (DRIE) technique. The PDMS base and curing agent were mixed at a weight ratio of 10:1. After degassing in a vacuum chamber, the mixture was casted using the master Si mold and degassed again. Next, the master silicon substrate with PDMS was placed inside to pre-heated convection oven at 80 °C for 2 h. Once cured, PDMS stamp with microstructures was carefully peeled off. The details of the process steps and mechanism are discussed in results section.

ZnO Nanowire-Based Field Effect Transistor (NW-FET): The fabrication of back-gated ZnO NW-FETs was performed following conventional microfabrication processes including photolithography and metal deposition (Ti (10 nm)/Au (90 nm)) for source and drain contacts using e-beam evaporation method and lift-off. Highly doped silicon with 200 nm thick SiO$_2$ was used as the gate and gate dielectric, respectively.

EHD Printing: To fabricate printed PDs, the contact electrodes were realized over the aligned NWs using an electrohydrodynamic (EHD) printer (super inkjet (SIJ^R)). The printed ink is commercial gold ink (CAu-2000). A thermal treatment is applied to the substrate at 100 °C for 10 minutes prior to printing. The printing is performed using a 75% sine wave, 300 V amplitude, 0 DC bias, 80 Hz frequency, and the stage speed of 0.5 mm s^{-1}. To increase the conductivity of the printed lines, the same pattern is repeated over five layers. The curing step is performed at 250 °C for 2 h.

Electrical and Optoelectrical Characterizations: The electrical characterization of ZnO NW-FETs and printed PDs such as time resolved photoresponse and IV characteristics were performed in the ambient environment using semiautomated summit 12k Auto prober and semiconductor device parameter analyzer (B1500A, Agilent). A UV light emitting diode (LED) with the wavelength of 365nm was used for evaluating photodetection capabilities of the fabricated devices.

Supporting Information

Supporting Information is available from the Wiley Online Library or from the author.

Conflict of Interest

The authors declare no conflict of interest.

Data Availability Statement

The data that support the findings of this study are available from the corresponding author upon reasonable request.

[1] J. Sun, A. Sapkota, H. Park, P. Wesley, Y. Jung, B. B. Maskey, Y. Kim, Y. Majima, J. Ding, J. Ouyang, C. Guo, J. Lefebvre, Z. Li, P. R. L. Malenfant, A. Javey, G. Cho, *Adv. Electron. Mater.* **2020**, *6*, 1901431.

[2] a) O. Ozioko, P. Karipoth, P. Escobedo, M. Ntagios, A. Pullanchiyodan, R. Dahiya, *Adv. Intell. Syst.* **2021**, *3*, 1900145; b) P. Karipoth, A. Christou, A. Pullanchiyodan, R. Dahiya, *Adv. Intell. Syst.* **2021**, *4*, 2100092; c) Y. Zhang, M. Peng, Y. Liu, T. Zhang, Q. Zhu, H. Lei, S. Liu, Y. Tao, L. Li, Z. Wen, X. Sun, *ACS Appl. Mater. Interfaces* **2020**, *12*, 19384; d) A. S. Dahiya, T. Gil, J. Thireau, N. Azemard, A. Lacampagne, B. Charlot, A. Todri-Sanial, *Adv. Electron. Mater.* **2020**, *6*, 2000547; e) Y. Kumaresan, S. Ma, O. Ozioko, R. Dahiya, *IEEE Sens. J.* **2022**, *22*, 3974.

[3] a) O. Ozioko, R. Dahiya, *Adv. Intell. Syst.* **2022**, *4*, 2100091; b) F. Nikbakhtnasrabadi, H. El Matbouly, M. Ntagios, R. Dahiya, *ACS Appl. Electron. Mater.* **2021**, *3*, 2233.

[4] a) A. Chhetry, S. Sharma, S. C. Barman, H. Yoon, S. Ko, C. Park, S. Yoon, H. Kim, J. Y. Park, *Adv. Funct. Mater.* **2021**, *31*, 2007661; b) K. Sanderson, *Nature* **2021**, *591*, 685; c) P. Escobedo, M. Ntagios, D. Shakthivel, W. T. Navaraj, R. Dahiya, *IEEE Trans. Rob.* **2021**, *37*, 683; d) R. Dahiya, D. Akinwande, J. S. Chang, *Proc. IEEE* **2019**, *107*, 2011.

[5] W.-H. Yeo, Y.-S. Kim, J. Lee, A. Ameen, L. Shi, M. Li, S. Wang, R. Ma, S. H. Jin, Z. Kang, Y. Huang, J. A. Rogers, *Adv. Mater.* **2013**, *25*, 2773.

[6] a) A. S. Dahiya, J. Thireau, J. Boudaden, S. Lal, U. Gulzar, Y. Zhang, T. Gil, N. Azemard, P. Ramm, T. Kiessling, C. O'Murchu, F. Sebelius, J. Tilly, C. Glynn, S. Geary, C. O'Dwyer, K. M. Razeeb, A. Lacampagne, B. Charlot, A. Todri-Sanial, *J. Electrochem. Soc.* **2020**, *167*, 037516; b) P. Escobedo, M. Bhattacharjee, F. Nikbakhtnasrabadi, R. Dahiya, *IEEE Internet of Things J.* **2021**, *8*, 5093.

[7] a) J. Biggs, J. Myers, J. Kufel, E. Ozer, S. Craske, A. Sou, C. Ramsdale, K. Williamson, R. Price, S. White, *Nature* **2021**, *595*, 532; b) E. Ozer, J. Kufel, J. Myers, J. Biggs, G. Brown, A. Rana, A. Sou, C. Ramsdale, S. White, *Nat. Electron.* **2020**, *3*, 419.

ADVANCED
SCIENCE NEWS
www.advancedsciencenews.com

ADVANCED
ELECTRONIC
MATERIALS
www.advelectronicmat.de

[8] M. S. Baghini, A. Vilouras, R. Dahiya, *IEEE Trans. Biomed. Circuits Syst.* **2021**, *15*, 1174.

[9] a) S. Ma, Y. Kumaresan, A. S. Dahiya, L. Lorenzelli, R. Dahiya, *IEEE Sens. J.* **2022**, https://doi.org/10.1109/JSEN.2022.3140651; b) S. Ma, Y. Kumaresan, A. S. Dahiya, R. Dahiya, *Adv. Electron. Mater.* **2021**, https://doi.org/10.1002/aelm.202101029.

[10] a) L. Migliorini, C. Piazzoni, K. Pohako-Esko, M. Di Girolamo, A. Vitaloni, F. Borghi, T. Santaniello, A. Aabloo, P. Milani, *Adv. Funct. Mater.* **2021**, *31*, 2102180; b) E. S. Hosseini, S. Dervin, P. Ganguly, R. Dahiya, *ACS Appl. Bio Mater.* **2021**, *4*, 163; c) N. Yogeswaran, E. S. Hosseini, R. Dahiya, *ACS Appl. Mater. Interfaces* **2020**, *12*, 54035; d) M. A. Kafi, A. Paul, A. Vilouras, R. Dahiya, *Biosens. Bioelectron.* **2020**, *147*, 111781; e) A. S. Dahiya, D. Shakthivel, Y. Kumaresan, A. Zumeit, A. Christou, R. Dahiya, *Nano Convergence* **2020**, *7*, 33; f) N. L. Vaklev, J. H. G. Steinke, A. J. Campbell, *Adv. Mater. Interfaces* **2019**, *6*, 1900173; g) S. Khan, L. Lorenzelli, R. S. Dahiya, *IEEE Sens. J.* **2015**, *15*, 3164.

[11] a) A. Zumeit, A. S. Dahiya, A. Christou, D. Shakthivel, R. Dahiya, *npj Flexible Electron* **2021**, *5*, 18; b) A. Zumeit, A. S. Dahiya, A. Christou, R. Dahiya, *Jpn. J. Appl. Phys.* **2021**, 61; c) A. Zumeit, W. T. Navaraj, D. Shakthivel, R. Dahiya, *Adv. Electron. Mater.* **2020**, *6*, 1901023; d) C. Linghu, S. Zhang, C. Wang, J. Song, *npj Flexible Electron.* **2018**, *2*, 26; e) J. A. Rogers, M. G. Lagally, R. G. Nuzzo, *Nature* **2011**, *477*, 45.

[12] a) B. Yoo, S. Cho, S. Seo, J. Lee, *ACS Appl. Mater. Interfaces* **2014**, *6*, 19247; b) S. Kim, J. Wu, A. Carlson, S. H. Jin, A. Kovalsky, P. Glass, Z. Liu, N. Ahmed, S. L. Elgan, W. Chen, *Proc. Natl. Acad. Sci. USA* **2010**, *107*, 17095.

[13] a) Z. Yan, T. Pan, M. Xue, C. Chen, Y. Cui, G. Yao, L. Huang, F. Liao, W. Jing, H. Zhang, *Adv. Sci.* **2017**, *4*, 1700251; b) X. Feng, H. Cheng, A. M. Bowen, A. W. Carlson, R. G. Nuzzo, J. A. Rogers, *J. Appl. Mech.* **2013**, *80*, 061023; c) M. A. Meitl, Z.-T. Zhu, V. Kumar, K. J. Lee, X. Feng, Y. Y. Huang, I. Adesida, R. G. Nuzzo, J. A. Rogers, *Nat. Mater.* **2006**, *5*, 33.

[14] J. Bian, L. Zhou, X. Wan, C. Zhu, B. Yang, Y. Huang, *Adv. Electron. Mater.* **2019**, *5*, 1800900.

[15] L. Johnston, J. Yang, J. Han, K. Kalantar-Zadeh, J. Tang, *J. Mater. Chem. C* **2022**, *10*, 921.

[16] Y. Huang, N. Zheng, Z. Cheng, Y. Chen, B. Lu, T. Xie, X. Feng, *ACS Appl. Mater. Interfaces* **2016**, *8*, 35628.

[17] H. Luo, C. Wang, C. Linghu, K. Yu, C. Wang, J. Song, *Natl. Sci. Rev.* **2020**, *7*, 296.

[18] a) H. Luo, S. Wang, C. Wang, C. Linghu, J. Song, *Adv. Funct. Mater.* **2021**, *31*, 2010297; b) W. T. Navaraj, S. Gupta, L. Lorenzelli, R. Dahiya, *Adv. Electron. Mater.* **2018**, *4*, 1700277.

[19] S. Acharya, A. B. Panda, N. Belman, S. Efrima, Y. Golan, *Adv. Mater.* **2006**, *18*, 210.

[20] a) A. Christou, F. Liu, R. Dahiya, *Microsyst. Nanoeng.* **2021**, *7*, 98; b) C. García Núñez, F. Liu, W. T. Navaraj, A. Christou, D. Shakthivel, R. Dahiya, *Microsyst. Nanoeng.* **2018**, *4*, 22; c) A. Javey, Nam, R. S. F. , H. Yan, C. M. Lieber, *Nano Lett.* **2007**, *7*, 773.

[21] D. Shakthivel, M. Ahmad, M. R. Alenezi, R. Dahiya, S. R. P. Silva, *1D Semiconducting Nanostructures for Flexible and Large-Area Electronics*, Cambridge University Press, Cambridge **2019**.

[22] E. Mullen, M. A. Morris, *Nanomaterials* **2021**, *11*, 1085.

[23] Z. Fan, J. C. Ho, Z. A. Jacobson, H. Razavi, A. Javey, *Proc. Natl. Acad. Sci. USA* **2008**, *105*, 11066.

[24] Z. Fan, J. C. Ho, Z. A. Jacobson, R. Yerushalmi, R. L. Alley, H. Razavi, A. Javey, *Nano Lett.* **2008**, *8*, 20.

[25] a) Q. Lei, J. He, D. Li, *Nanoscale* **2019**, *11*, 15195; b) P. Galliker, J. Schneider, H. Eghlidi, S. Kress, V. Sandoghdar, D. Poulikakos, *Nat. Commun.* **2012**, *3*, 890; c) J.-U. Park, M. Hardy, S. J. Kang, K. Barton, K. Adair, D. k. Mukhopadhyay, C. Y. Lee, M. S. Strano, A. G. Alleyne, J. G. Georgiadis, P. M. Ferreira, J. A. Rogers, *Nat. Mater.* **2007**, *6*, 782.

[26] A. S. Dahiya, C. Opoku, D. Alquier, G. Poulin-Vittrant, F. Cayrel, O. Graton, L.-P. T. H. Hue, N. Camara, *Nanoscale Res. Lett.* **2014**, *9*, 379.

[27] N. E. Persson, J. Rafshoon, K. Naghshpour, T. Fast, P.-H. Chu, M. McBride, B. Risteen, M. Grover, E. Reichmanis, *ACS Appl. Mater. Interfaces* **2017**, *9*, 36090.

[28] X. Ma, Q. Liu, D. Xu, Y. Zhu, S. Kim, Y. Cui, L. Zhong, M. Liu, *Nano Lett.* **2017**, *17*, 6961.

[29] S. Boubenia, A. S. Dahiya, G. Poulin-Vittrant, F. Morini, K. Nadaud, D. Alquier, *Sci. Rep.* **2017**, *7*, 15187.

[30] A. S. Dahiya, C. Opoku, G. Poulin-Vittrant, N. Camara, C. Daumont, E. G. Barbagiovanni, G. Franzò, S. Mirabella, D. Alquier, *ACS Appl. Mater. Interfaces* **2017**, *9*, 573.

[31] F. Léonard, A. A. Talin, *Nat. Nanotechnol.* **2011**, *6*, 773.

[32] Y. Kumaresan, G. Min, A. S. Dahiya, A. Ejaz, D. Shakthivel, R. Dahiya, *Adv. Mater. Technol.* **2021**, *7*, 2100804.

[33] a) S. Veeralingam, L. Durai, P. Yadav, S. Badhulika, *ACS Appl. Electron. Mater.* **2021**, *3*, 1162; b) Y. Liu, L. Du, G. Liang, W. Mu, Z. Jia, M. Xu, Q. Xin, X. Tao, A. Song, *IEEE Electron Device Lett.* **2018**, *39*, 1696.

[34] a) J. Kim, H. Park, S.-H. Jeong, *J. Ind. Eng. Chem.* **2020**, *82*, 144; b) B. Cook, M. Gong, A. Corbin, D. Ewing, A. Tramble, J. Wu, *ACS Omega* **2019**, *4*, 22497; c) C. G. Núñez, A. Vilouras, W. T. Navaraj, F. Liu, R. Dahiya, *IEEE Sens. J.* **2018**, *18*, 7881; d) D.-H. Lien, H.-P. Wang, S.-B. Chen, Y.-C. Chi, C.-L. Wu, G.-R. Lin, Y.-C. Liao, J.-H. He, *npj Flexible Electron.* **2018**, *2*, 19; e) Y. Li, Y. Li, J. Chen, Z. Sun, Z. Li, X. Han, P. Li, X. Lin, R. Liu, Y. Ma, W. Huang, *J. Mater. Chem. C* **2018**, *6*, 11666; f) A. A. Gupta, S. Arunachalam, S. G. Cloutier, R. Izquierdo, *ACS Photonics* **2018**, *5*, 3923; g) B. Zhao, F. Wang, H. Chen, L. Zheng, L. Su, D. Zhao, X. Fang, *Adv. Funct. Mater.* **2017**, *27*, 1700264; h) T. Q. Trung, V. Q. Dang, H.-B. Lee, D.-I. Kim, S. Moon, N.-E. Lee, H. Lee, *ACS Appl. Mater. Interfaces* **2017**, *9*, 35958; i) W. Peng, X. Wang, R. Yu, Y. Dai, H. Zou, A. C. Wang, Y. He, Z. L. Wang, *Adv. Mater.* **2017**, *29*, 1606698; j) C.-H. Lin, D.-S. Tsai, T.-C. Wei, D.-H. Lien, J.-J. Ke, C.-H. Su, J.-Y. Sun, Y.-C. Liao, J.-H. He, *ACS Nano* **2017**, *11*, 10230; k) M. Gong, Q. Liu, B. Cook, B. Kattel, T. Wang, W.-L. Chan, D. Ewing, M. Casper, A. Stramel, J. Z. Wu, *ACS Nano* **2017**, *11*, 4114; l) Z. Wang, R. Yu, X. Wang, W. Wu, Z. L. Wang, *Adv. Mater.* **2016**, *28*, 6880; m) Y. Dong, Y. Zou, J. Song, Z. Zhu, J. Li, H. Zeng, *Nano Energy* **2016**, *30*, 173; n) N. Nasiri, R. Bo, F. Wang, L. Fu, A. Tricoli, *Adv. Mater.* **2015**, *27*, 4336; o) X. Liu, L. Gu, Q. Zhang, J. Wu, Y. Long, Z. Fan, *Nat. Commun.* **2014**, *5*, 4007; p) G. Cheng, X. Wu, B. Liu, B. Li, X. Zhang, Z. Du, *Appl. Phys. Lett.* **2011**, *99*, 203105; q) Q. Yang, X. Guo, W. Wang, Y. Zhang, S. Xu, D. H. Lien, Z. L. Wang, *ACS Nano* **2010**, *4*, 6285; r) T. Chen, X. Gao, J.-Y. Zhang, J.-L. Xu, S.-D. Wang, *Adv. Opt. Mater.* **2020**, *8*, 1901289; s) Z. Jin, Q. Zhou, Y. Chen, P. Mao, H. Li, H. Liu, J. Wang, Y. Li, *Adv. Mater.* **2016**, *28*, 3697.

[35] A. S. Dahiya, C. Opoku, C. Oshman, G. Poulin-Vittrant, F. Cayrel, L.-P. T. H. Hue, D. Alquier, N. Camara, *Appl. Phys. Lett.* **2015**, *107*, 033105.

[36] S. Oh, C.-K. Kim, J. Kim, *ACS Photonics* **2018**, *5*, 1123.

[37] L. Liu, C. Yang, A. Patanè, Z. Yu, F. Yan, K. Wang, H. Lu, J. Li, L. Zhao, *Nanoscale* **2017**, *9*, 8142.

[38] A. Aldalbahi, E. Li, M. Rivera, R. Velazquez, T. Altalhi, X. Peng, P. X. Feng, *Sci. Rep.* **2016**, *6*, 23457.

[39] A. A. La Mattina, S. Mariani, G. Barillaro, *Adv. Sci.* **2020**, *7*, 1902872.

[40] D. Shakthivel, W. T. Navaraj, S. Champet, D. H. Gregory, R. S. Dahiya, *Nanoscale Adv.* **2019**, *1*, 3568.